Thiosulfate species promoting hydrogen evolution reaction at the heterointerface of Ir clusters-loaded WS_2 nanosheets

Sho Kitano, Reiko Tagusari, Takeharu Sugiyama, Yuta Nagasaka, Naoto Wakabayashi, Rioto Wada, Tomoya Nagao, Mana Iwai, Koji Fushimi, Yoshitaka Aoki, Hiroki Habazaki**

*Sho Kitano: Division of Applied Chemistry, Faculty of Engineering, Hokkaido University, Sapporo, Hokkaido 060-8628, Japan

Reiko Tagusari: Graduate School of Chemical Sciences and Engineering, Hokkaido University, Sapporo, Hokkaido 060-8628, Japan

Takeharu Sugiyama: Research Center for Synchrotron Light Applications, Kyushu University, 6-1 Kasuga-koen, Kasuga, Fukuoka 816-8580, Japan

Yuta Nagasaka: Graduate School of Chemical Sciences and Engineering, Hokkaido University, Sapporo, Hokkaido 060-8628, Japan

Naoto Wakabayashi: Graduate School of Chemical Sciences and Engineering, Hokkaido University, Sapporo, Hokkaido 060-8628, Japan

Rioto Wada: Graduate School of Chemical Sciences and Engineering, Hokkaido University, Sapporo, Hokkaido 060-8628, Japan

Tomoya Nagao: Graduate School of Chemical Sciences and Engineering, Hokkaido University, Sapporo, Hokkaido 060-8628, Japan

Mana Iwai: Division of Applied Chemistry, Faculty of Engineering, Hokkaido University, Sapporo, Hokkaido 060-8628, Japan

Koji Fushimi: Division of Applied Chemistry, Faculty of Engineering, Hokkaido University, Sapporo, Hokkaido 060-8628, Japan

Yoshitaka Aoki: Division of Applied Chemistry, Faculty of Engineering, Hokkaido University, Sapporo, Hokkaido 060-8628, Japan

*Hiroki Habazaki: Division of Applied Chemistry, Faculty of Engineering, Hokkaido University, Sapporo, Hokkaido 060-8628, Japan

Experimental

1. Sample preparation

All chemicals were used as received without further purification. Ammonium tetrathiotungstate ($(NH_4)_2WS_4$) (1.5 mmol, Sigma-Aldrich) was dispersed in a mixed solvent of oleylamine (14 cm^3, Fujifilm Wako Pure Chemical Corporation) and 1-octadecene (16 cm^3, Tokyo Chemical Industry Co., Ltd.) in a three-necked flask. The mixture was stirred for 5 min and degassed under an Ar atmosphere at 110°C for 30 min. The solution was then heated to 270°C for 5 min under Ar, resulting in a suspension of monolayer WS_2. The suspension was centrifuged at 6000 rpm for 10 min to obtain a black precipitate, and the precipitate was washed by acetone three times. The precipitate was dried in vacuo and monolayer WS_2 nanosheet was prepared. For the preparation of Ir clusters, iridium(III) chloride hydrate ($IrCl_3 \cdot 3H_2O$) (1.76 mmol, Kanto Chemical Co., Inc.) was dissolved in a mixed solvent of ethylene glycol (240 cm^3, Kanto Chemical Co., Inc.) and ultrapure water (160 cm^3). The solution was heated to 140°C for 3 h under atmospheric conditions using an oil bath with stirring. After cooling to room temperature, the colloidal suspension of Ir clusters were obtained. To combine monolayer WS_2 nanosheets with Ir clusters, the prepared WS_2 (40 mg) was dispersed in 40 cm^3 of acetylacetone (Kanto Chemical Co., Inc.) by ultrasonication for 30 min. The dispersion was then stirred while 40 cm^3 of the previously synthesized Ir cluster suspension was added dropwise at a rate of 4 cm^3 min^{-1}. Then, 120 cm^3 of ultrapure water was added dropwise at a rate of 4 cm^3 min^{-1}. After dropwise addition, the mixture was allowed to stand for 20 min, during which time the mixture separated into a black top layer and a transparent bottom layer. The 5 cm^3 of the upper layer was collected, mixed with 35 cm^3 of pure water, and centrifuged at 6000 rpm for 10 min to precipitate a black material. The supernatant was discarded, and the process was repeated by adding another 5 cm^3 of the upper layer until no upper layer remained.

The sample was dried in vacuo. Ir clusters were similarly deposited on graphene (Aldrich). The graphene catalyst loaded with Ir clusters (Ir/G) was synthesized using the same procedure, except that WS_2 was replaced with graphene.

2. Characterization

The morphology and elemental analysis of the prepared samples were analyzed using a low acceleration scanning electron microscopy (SEM, Sigma 500, ZEISS) with energy dispersive spectroscopy (EDS). Powder samples were placed directly on carbon tape and vacuum dried overnight. The acceleration voltage was set at 1.5 kV. The nanostructures of prepared samples were observed by transmission electron microscopy (TEM, JEM-2010, JEOL Ltd.) with 200 kV acceleration voltage. Elemental analysis and microstructure examination of the samples were performed by scanning transmission electron microscopy (STEM, JEM-ARM200F, JEOL Ltd.). X-ray Diffraction (XRD) analysis was performed using a Rigaku Ultima IV to determine the crystal structure of the samples. A Cu-Kα radiation source ($\lambda = 0.15418$ nm) was used with a tube voltage of 40 kV and 20 mA. The morphology analysis of the prepared sample was performed using atomic force microscopy (AFM, SPA-400, Hitachi High-Tech Co.). X-ray Photoelectron Spectroscopy (XPS, JEOL-JPS9010MC, JEOL Ltd.) analysis was performed to measure the surface composition of the prepared samples. Binding energies were corrected by referring to the C 1s binding energy of the carbon atoms of the ligand in the specimens at 284.5 eV. Data fitting was performed using XPSPEAK41. X-ray fluorescence (XRF, JSX-3100RII, JEOL Ltd.) analysis was used to determine the concentration of Ir clusters suspension. X-ray absorption fine structure (XAFS) spectra were obtained in transmission mode for W L_3 and Ir L_3-edge spectra and in

fluorescence mode for S-K edge spectra using Kyushu University Beamline (BL06) at SAGA-LS (Saga, Japan) with the storage ring operating at 1.4 GeV. The energy range of this light source (bending magnet) was 2.1-23 keV. A silicon (111) double crystal monochromator was used to obtain the incident X-ray beam. The typical photon flux was 10^{10} photons s^{-1}. The fluorescence X-ray intensities were monitored with a silicon drift detector. *In-situ* XAFS measurements were carried out in transmission mode for W L_3 and Ir L_3-edge spectra and in fluorescence mode for S-K edge spectra. The measurements were performed by employing a three-electrode system connected to a HZ-7000 potentiostat (Meiden Hokuto) using a laboratory-prepared polyetheretherketone cell with a measurement window of 0.5×1.0 cm^2 at side walls where a Kapton films (7.5 μm thickness) covered the whole window area. The electrolyte was 1 mol L^{-1} phosphate buffer solution (PBS), and Ag/AgCl was used as the reference electrode and Pt foil as the counter electrode. All potentials were measured against the Ag/AgCl reference electrode, which has a potential of 0.198 V vs. the standard hydrogen electrode (SHE), and finally converted to a potential referring to the reversible hydrogen electrode (RHE). The synthesized catalyst samples were fixed on carbon paper and used as working electrodes. All measurements were carried out in an Ar atmosphere.

3. Electrochemical measurements

The ink for these electrodes was prepared by dispersing desired amount of the samples in 2 mL of acetylacetone using ultrasonication for 30 min. 5 μL of this ink was applied to a glassy carbon electrode to prepare the electrode. HER activities were evaluated using a rotating ring-disk electrode in a three-electrode system. The electrodes were used as the working electrode, and the

Ag/AgCl (under acidic and neutral conditions) or Hg/HgO (under alkaline condition) was used as the reference electrode, and a Pt counter electrode was used. The electrolytes were 0.5 mol dm^{-3} H_2SO_4 for the acidic condition, 1 mol dm^{-3} PBS for the neutral condition, or 1 mol dm^{-3} KOH for the alkaline condition at room temperature. Oxygen was removed by bubbling Ar gas for 15 min, and the electrode was rotated at 1600 rpm while the potential was swept from 0.5 V to -0.3 V vs. RHE at a sweep rate of 10 mV s^{-1} to evaluate the hydrogen evolution activity. Evaluations of OER activities were performed under the same condition, and the potential was swept from 1.1 V to 1.7 V vs. RHE at a sweep rate of 10 mV s^{-1}.

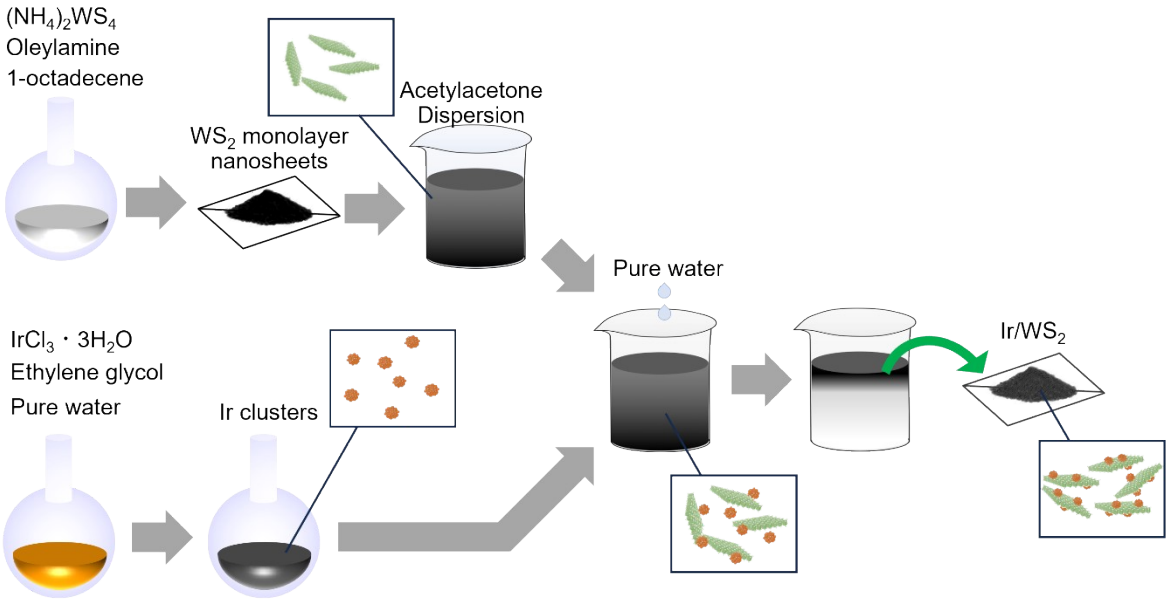

Fig. S1 Schematic illustration of the experimental procedure for fabrication of the Ir/WS_2.

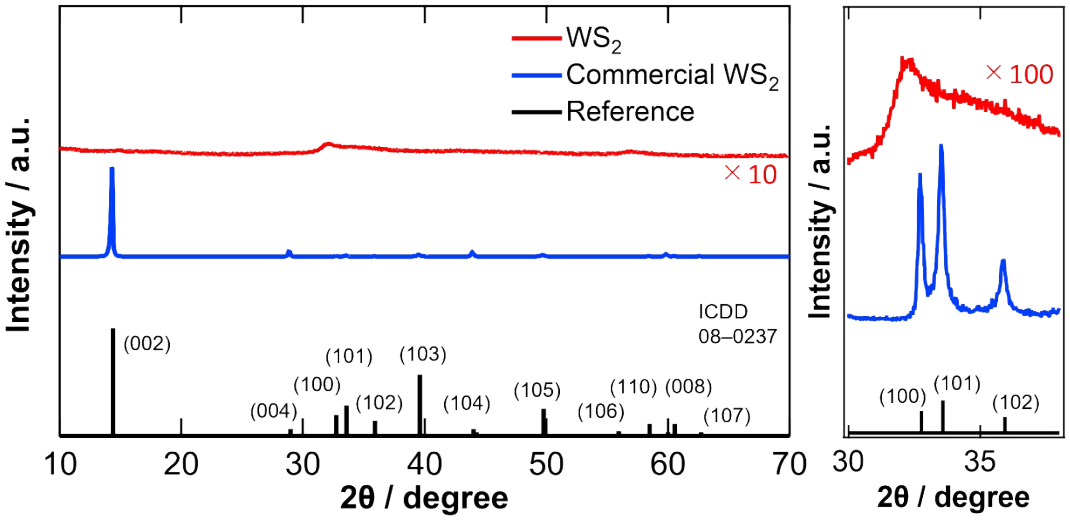

Fig. S2 XRD patterns of the monolayer WS_2 nanosheets and commercial bulk WS_2.

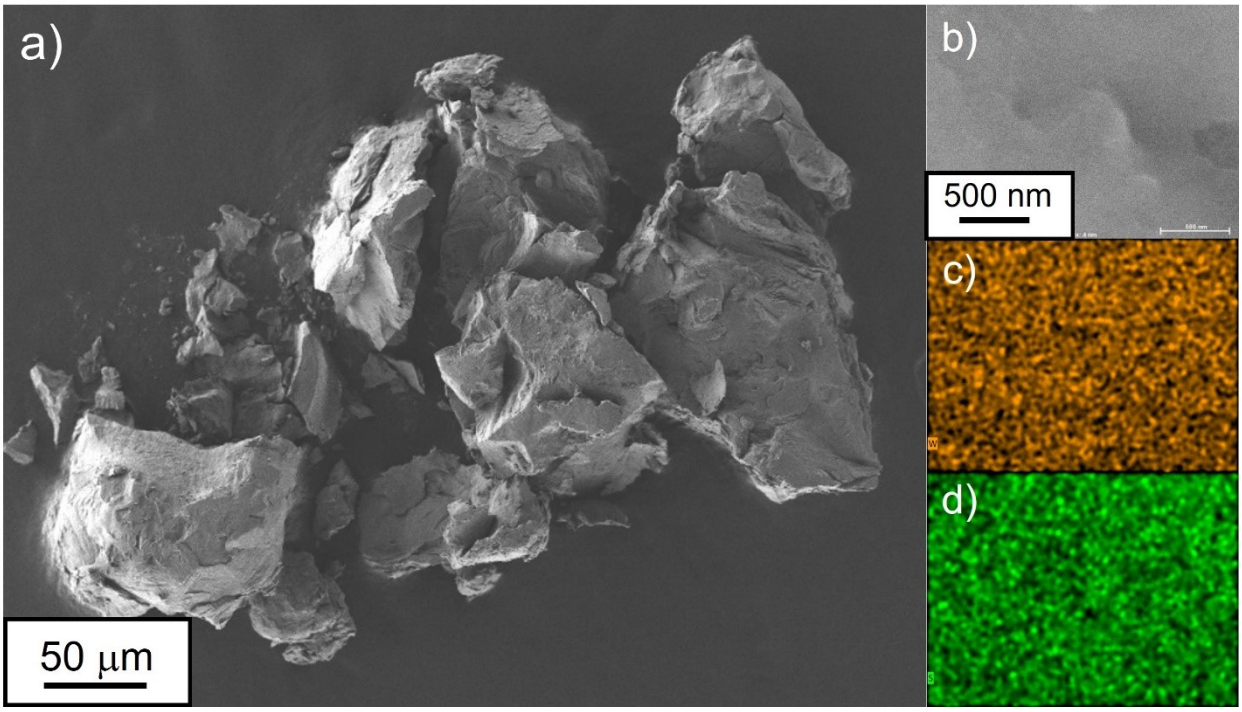

Fig. S3 (a), (b) SEM image of the aggregated powder of monolayer WS_2 nanosheets and EDX mappings of (c) W-M and (d) S-K.

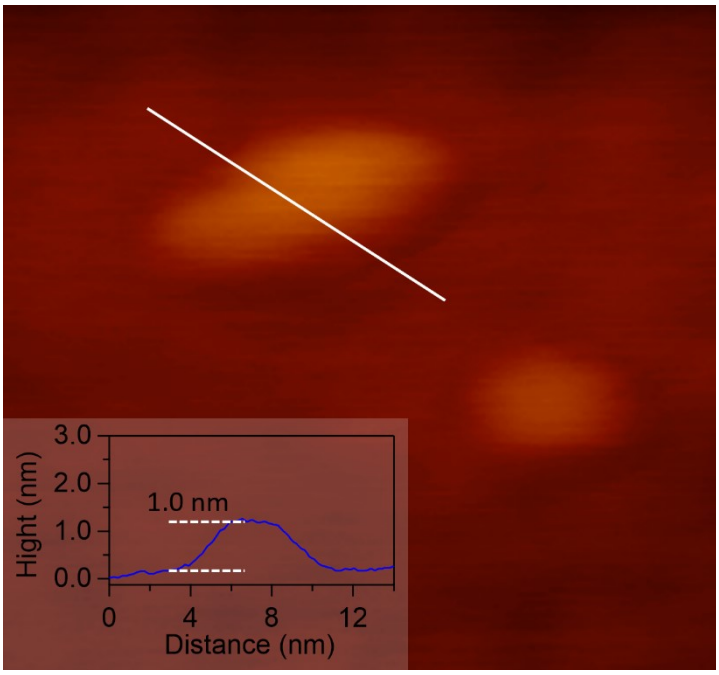

Fig. S4 AFM image of the monolayer WS_2 nanosheets. The inset shows the height profile of the white line.

The synthesized WS_2 showed a two-dimensional morphology with a thickness of approximately 1.0 nm, which was consistent with the results of previous studies on monolayer WS_2.[1] Thus, the synthesized WS_2 has the monolayer structure.

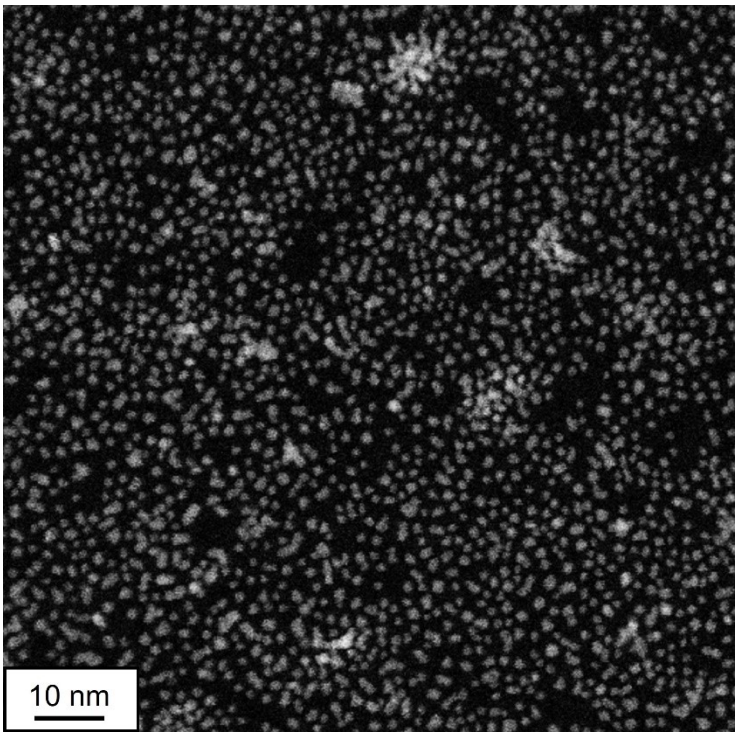

Fig. S5 Low magnification HAADF-STEM image of the Ir clusters

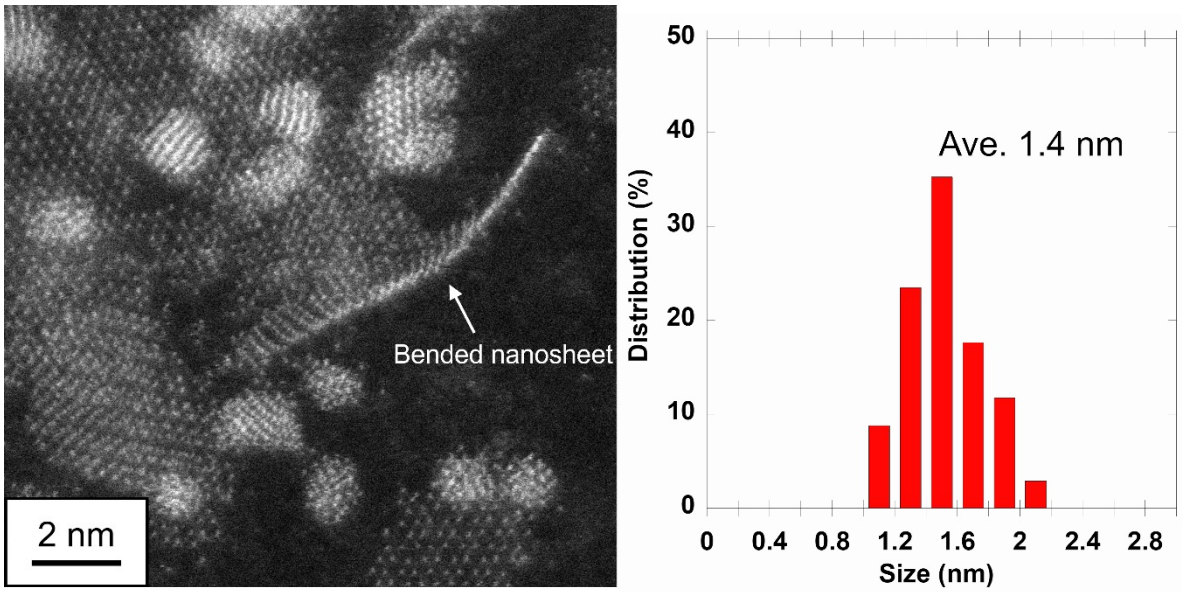

Fig. S6 HAADF-STEM image of the Ir/WS_2 with the bended monolayer WS_2 nanosheet and size distribution of the Ir clusters loaded on the WS_2.

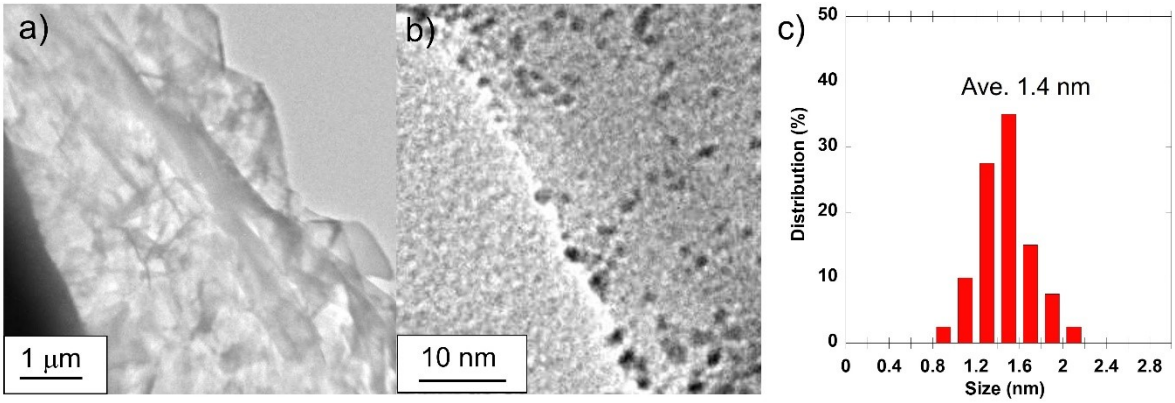

Fig. S7 TEM images of (a) the pristine graphene and (b) Ir/G. (c) Size distribution of Ir clusters loaded on the graphene

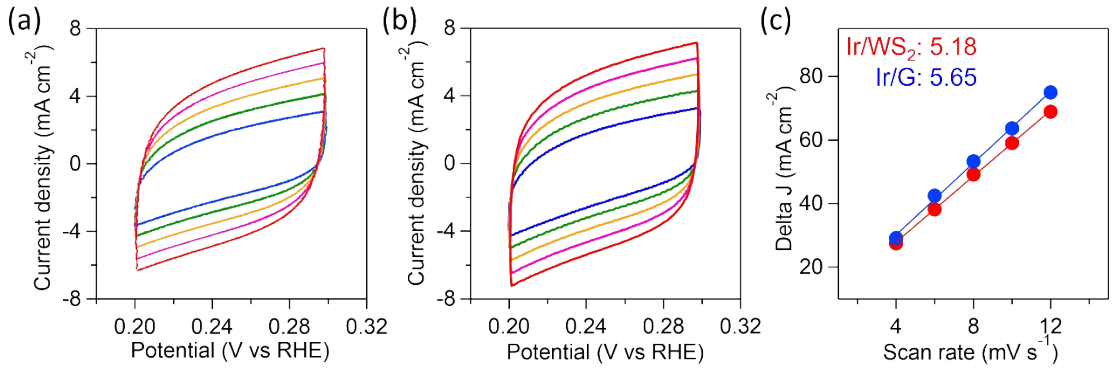

Fig. S8 CV curves of (a) Ir/WS_2 and (b) Ir/G at sweep rates from 4 mv s^{-1} to 12 mv s^{-1}. (c) Charging current density differences plotted against scan rate.

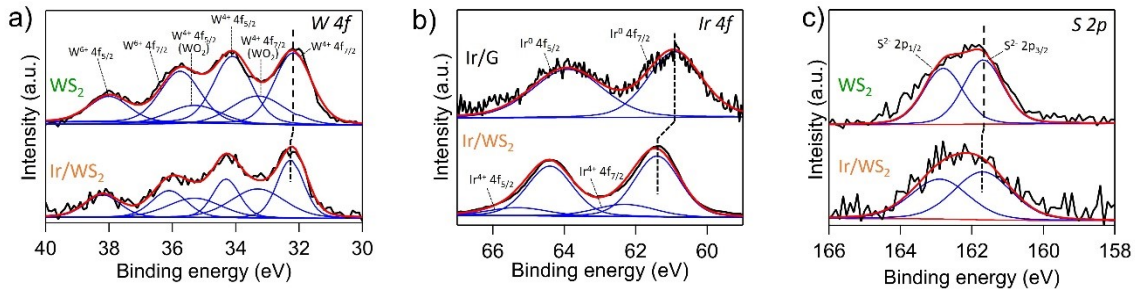

Fig. S9 XPS spectra for (a) W 4f, (b) Ir 4f and (c) S 2p of the pristine WS_2 and Ir/WS_2.

The pristine WS_2 showed the W $4f_{7/2}$ peak at 32.2 eV and S $2p_{3/2}$ peak at 161.7 eV , which are attributable to W^{4+} and S^{2-}, respectively (Fig. S7 (a) and (c)). The W $4f_{7/2}$ peaks attributable to W^{4+} (33.3 eV) and W^{6+} (35.8 eV) derived from tungsten oxides were also observed from deconvolution of the W 4f spectrum, indicating the partial formation of more oxidative states of W species than those of laminated WS_2 due to the extra high surface area of monolayer nanosheets. For the Ir/WS_2, the W 4f and S 2p spectra slightly changed to more oxidized states by combination with the Ir clusters, indicating slight oxidation of WS_2. The Ir $4f_{7/2}$ peaks in the Ir 4f spectra of Ir/WS_2 and Ir/G were observed at around 61 eV, which are similar to the peak energy of metallic Ir (60.8 eV) than that of IrO_2 (62.5 eV). This suggests that both the Ir clusters on WS_2 and graphene essentially have metallic states. When comparing the XPS spectra of the Ir 4f region for the Ir/WS_2 and the Ir/G, a notable peak shift towards the higher energy side was observed in the Ir $4f_{7/2}$ spectrum (61.4 eV) of the Ir/WS_2 catalyst compared to that of the Ir/G (60.7 eV) (Fig. S7 (b)). This shift suggests that the Ir clusters on the WS_2 nanosheet possess more oxidative states compared to those on graphene. The higher binding energy of Ir on WS_2 could be attributed to a stronger interaction between the Ir clusters and the WS_2 nanosheet, possibly due to the intrinsic electronic properties of the WS_2 surface.

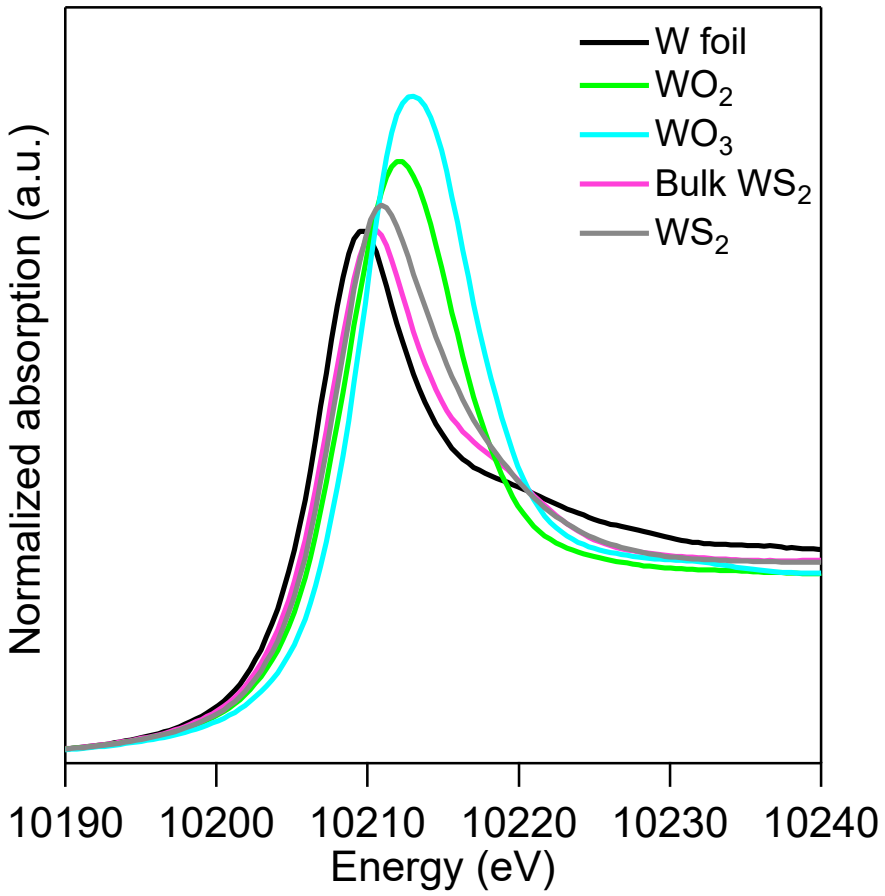

Fig. S10 W L_3-edge XANES spectra of the pristine WS_2 and reference compounds.

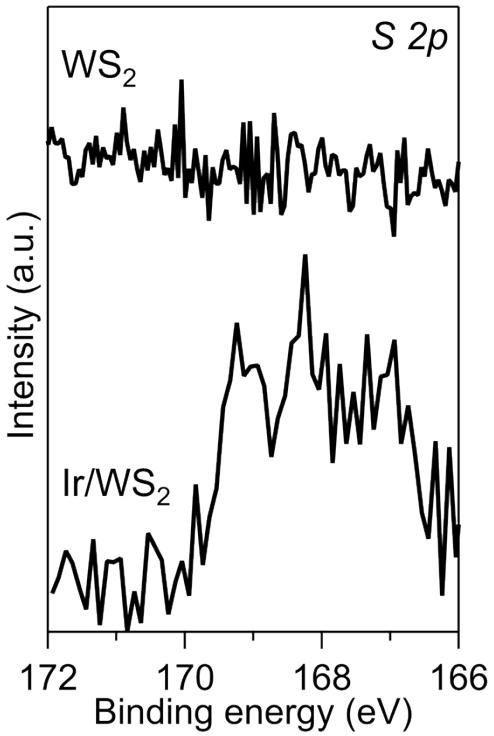

Fig. S11 XPS spectra for S 2p of the pristine WS_2 and Ir/WS_2 in the energy region of high-valent S species.

The Ir/WS_2 showed S $2p_{3/2}$ at the 168 eV assignable to S^{6+} while the pristine WS_2 showed no peak in the region, indicating that existence of thiosulfate species in the Ir/WS_2.

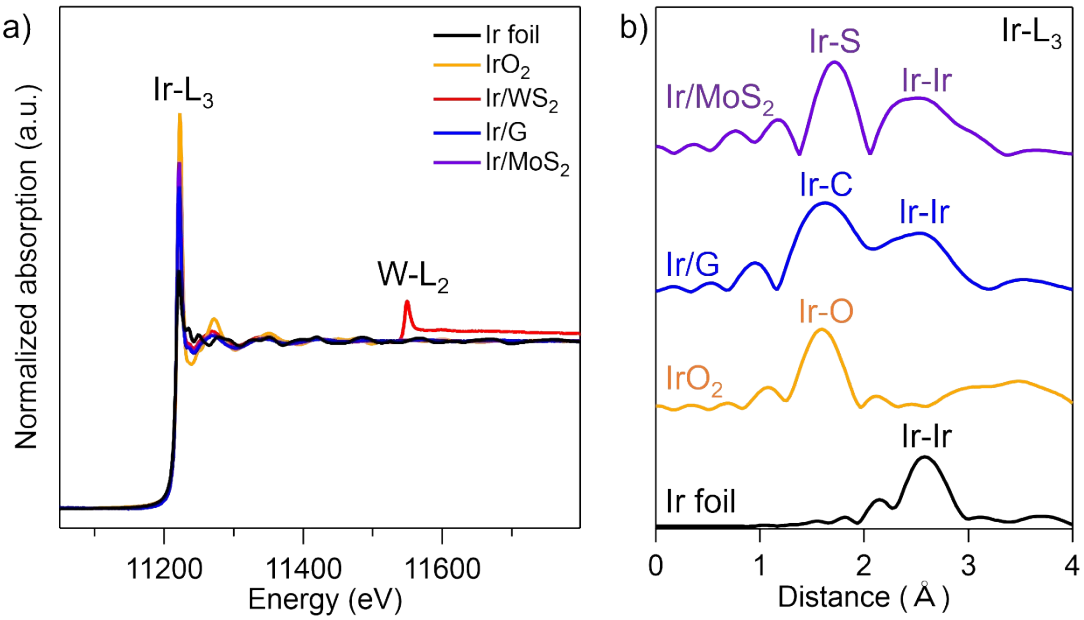

Fig. S12 (a) Ir L_3-edge and W L_2-edge XANES spectra and (b) FT of the k^3-weighted Ir L_3-edge EXAFS spectra of catalysts and reference samples.

We further investigated the heterointerfaces between Ir clusters and WS_2 using extended x-ray absorption fine structure (EXAFS) analysis. When metal clusters with diameters smaller than 3 nm form heterointerfaces with support materials, EXAFS peaks corresponding to bonds between surface atoms of the metal clusters and support elements appear in addition to those from metal-metal bonds within the cluster. In the case of Ir/WS_2, bonds were assumed to form between surface Ir atoms in the Ir clusters and S atoms in WS_2. However, due to the close energy of the Ir L_3 absorption edge and the W L_2 absorption edge, obtaining precise EXAFS results for Ir/WS_2 was not possible in this study. Therefore, we prepared Ir/MoS_2 composed of monolayer MoS_2 nanosheets instead of WS_2 and performed EXAFS analysis on Ir. The EXAFS analysis results for Ir/G, Ir/MoS_2, and the reference IrO_2 and Ir foil are shown in Fig. S1. For Ir foil, a peak corresponding to the Ir-Ir bond was observed at 2.7 Å, while for IrO_2, a peak corresponding to the Ir-O bond appeared at 1.5 Å. In the case of Ir/G, in addition to the Ir-Ir bond peak within the Ir clusters, an Ir-C bond peak, attributed to interactions between the C atoms of graphene and the surface Ir

atoms of the Ir clusters, was observed at 1.6 Å, consistent with previous reports.[2] Similarly, for Ir/MoS_2, along with the Ir-Ir bond peak from the Ir clusters, an additional peak corresponding to the bond between S atoms in the MoS_2 support and surface Ir atoms in the Ir clusters was observed at 1.9 Å, which is consistent with previous studies.[3] In this study, the peak positions corresponding to bonds between surface Ir atoms and support elements (S or C) at the heterointerfaces in Ir/WS_2 and Ir/G were clearly distinct. The presence of bonds between Ir atoms on the cluster surface and support elements, in addition to an Ir-Ir bond within the clusters, indicates that the composite catalyst forms chemical bonds between the support and the Ir clusters, establishing heterointerfaces. These results support the existence of a heterostructure in the Ir/WS_2.

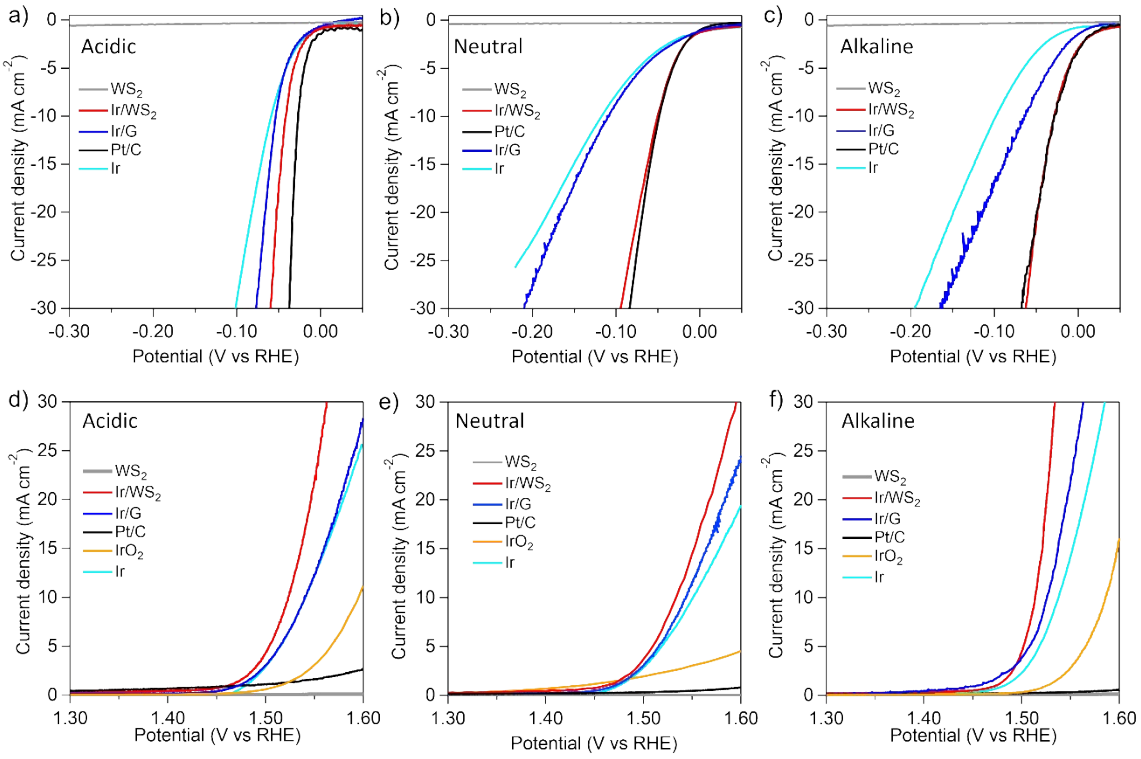

Fig. S13 IR-corrected polarization curves of the prepared catalysts, Pt/C and IrO_2 for (a)-(c) HER and (d)-(f) OER in the aqueous solution of (a), (d) 0.5 mol dm^{-3} H_2SO_4, (b), (e) 1 mol dm^{-3} PBS, and (c), (f) 1 mol dm^{-3} KOH.

The isolated Ir clusters showed similar activities to those of the Ir/G under all HER and OER conditions. When comparing the Ir/WS_2 and isolated Ir clusters, the activity discrepancy depending on the electrolyte condition in HER and similar activities in OER were also observed. The results were similar to those of the comparison between Ir/WS_2 with Ir/G, supporting the behaviors of thiosulfates in the Ir/WS_2. The slightly higher activities of Ir/G compared to isolated Ir clusters is probably due to the high dispersibility of the Ir clusters on the graphene support.

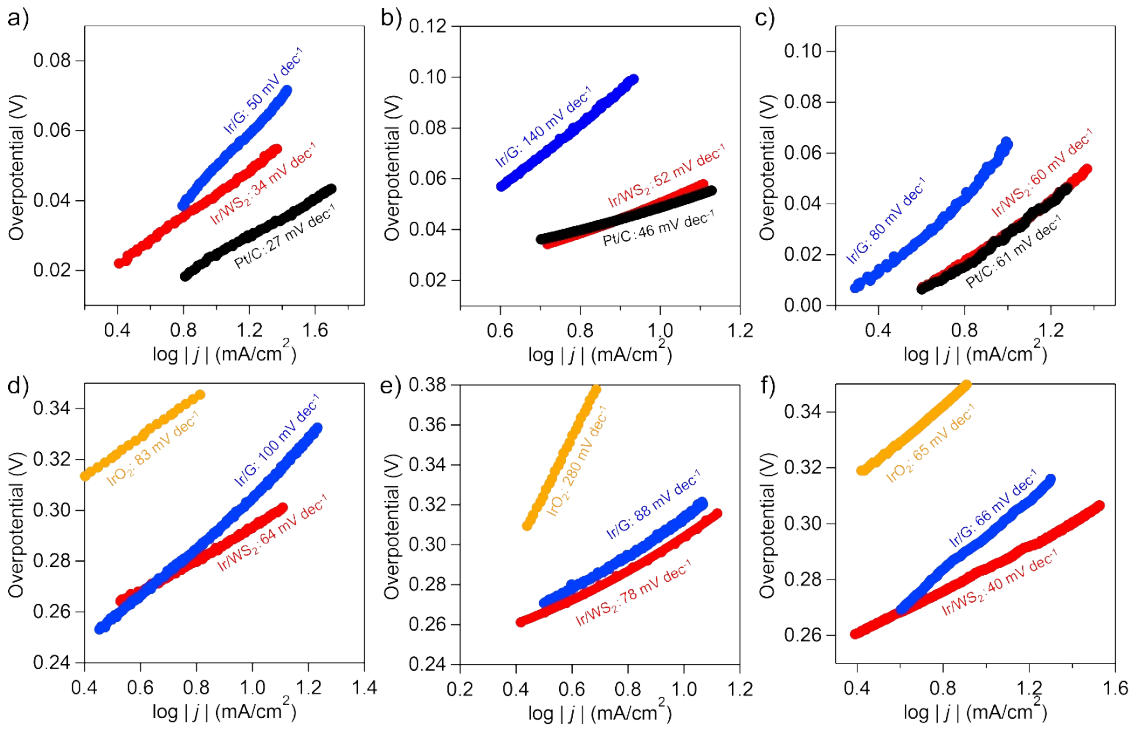

Fig. S14 Tafel slopes of the Ir/WS_2, Ir/G, Pt/C and IrO_2 for (a)-(c) HER and (d)-(f) OER in the aqueous solution of (a), (d) 0.5 mol dm^{-3} H_2SO_4, (b), (e) 1 mol dm^{-3} PBS, and (c), (f) 1 mol dm^{-3} KOH.

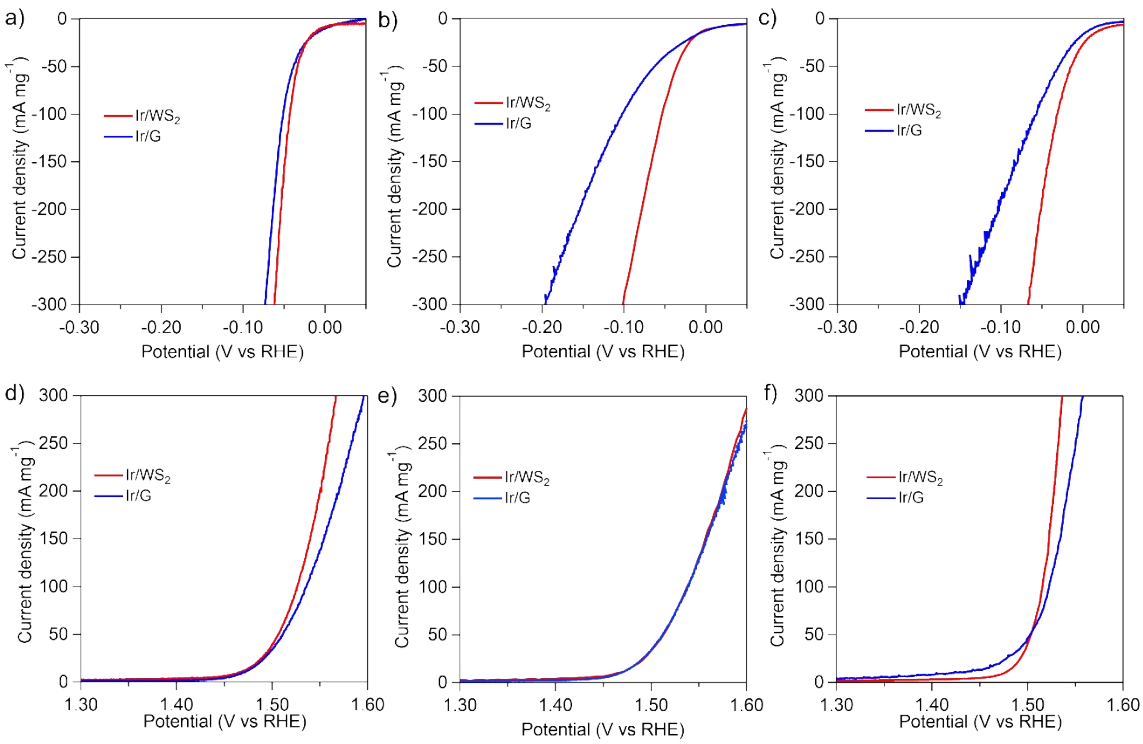

Fig. S15 IR-corrected polarization curves based on Ir mass of the Ir/WS_2 and Ir/G for (a)-(c) HER and (d)-(f) OER in the aqueous solution of (a), (d) 0.5 mol dm^{-3} H_2SO_4, (b), (e) 1 mol dm^{-3} PBS, and (c), (f) 1 mol dm^{-3} KOH.

The catalysts showed similar activity trends, i.e., the Ir/WS_2 showed much higher HER activities under neutral and alkaline conditions and the slightly higher HER activity compared to those of Ir/G. Therefore, we concluded that the activity discrepancy originated from the difference of WS_2 and graphene. The OER activities differed with pH, but the degree of difference in activities due to the difference in pH was smaller than the difference in activities in HER, which were similar results were also observed in OER.

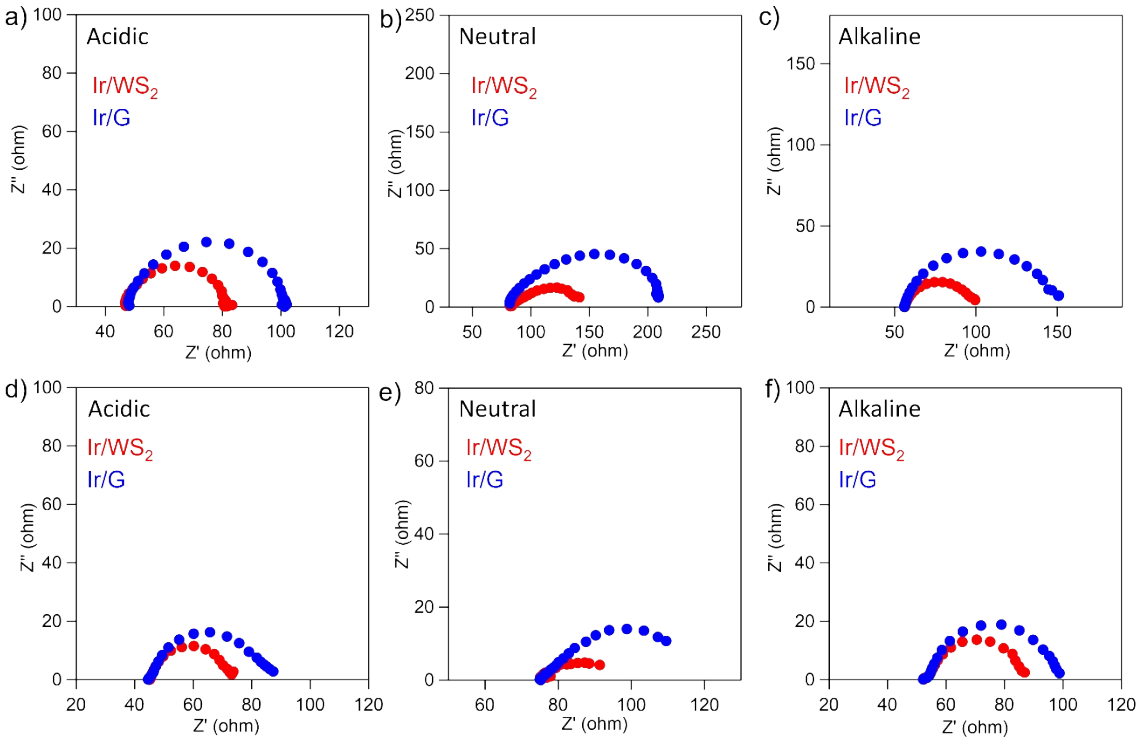

Fig. S16 Nyquist plots of the Ir/WS_2 and Ir/G for (a)-(c) HER and (d)-(f) OER in the aqueous solution of (a), (d) 0.5 mol dm^{-3} H_2SO_4, (b), (e) 1 mol dm^{-3} PBS, and (c), (f) 1 mol dm^{-3} KOH.

The Ir/WS_2 showed lower charge transfer resistances at the interface between electrolyte and catalyst than the Ir/G under all HER and OER conditions, indicating a faster transfer rate of the Ir/WS_2.

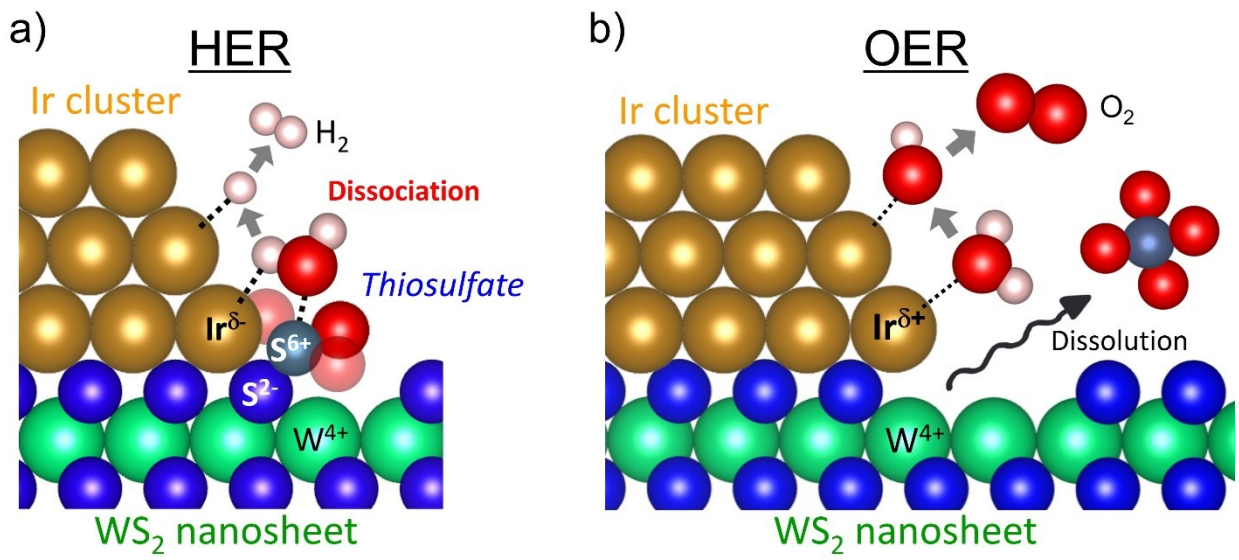

Fig. S17 Illustration of behaviors of thiosulfates at the heterointerface under (a) HER and (b) OER condition. Some O atoms are displayed translucently for easier viewing.

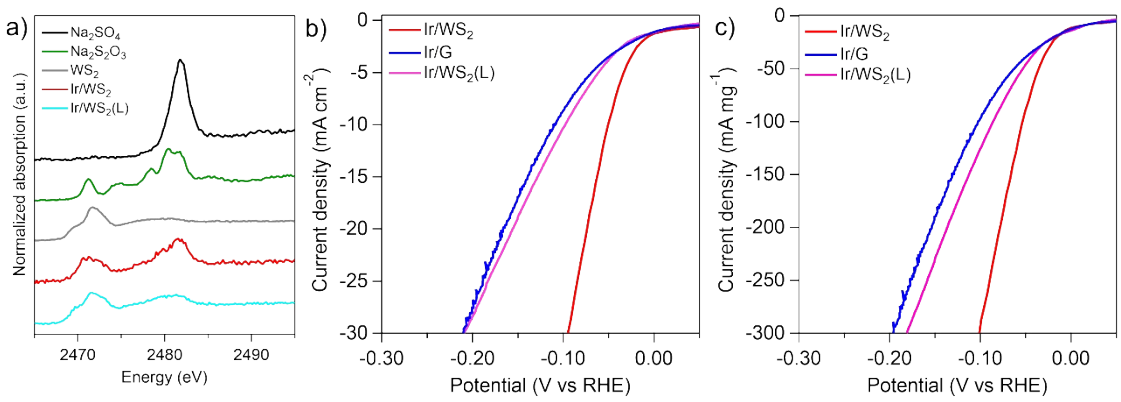

Fig. S18 (a) S K-edge XANES spectra of the pristine WS_2, Ir/WS_2, Ir/WS_2(L) and reference compounds. (b) (c) IR-corrected polarization curves of the Ir/WS_2, Ir/G and Ir/WS_2(L) for HER in the aqueous solution of 1 mol dm^{-3} PBS with current density per (b) geometric surface area and (c) Ir mass.

We also prepared the Ir/WS_2 catalyst with lower Ir content (58 wt%) to compare the original Ir/WS_2 (73 wt%) in the main text. The Ir/WS_2 with lower Ir content (Ir/WS_2 (L)) almost does not contain thiosulfate species, which was revealed by the XANES measurement (Fig. S18(a)). The Ir/WS_2 (L) showed lower HER activities than the original Ir/WS_2 even based on the Ir mass under the neutral condition. If the decrease in the intensity of S^{2-} peak and the increase in the intensity of S^{6+} peak for the original Ir/WS_2 observed in the in situ XAFS measurement corresponded to the oxidation of S^{2-} to SO_4^{2-}, both Ir/WS_2 catalysts should show similar catalytic activities. However, the observed difference in performance suggests that thiosulfate species play an important role in enhancing HER activities.

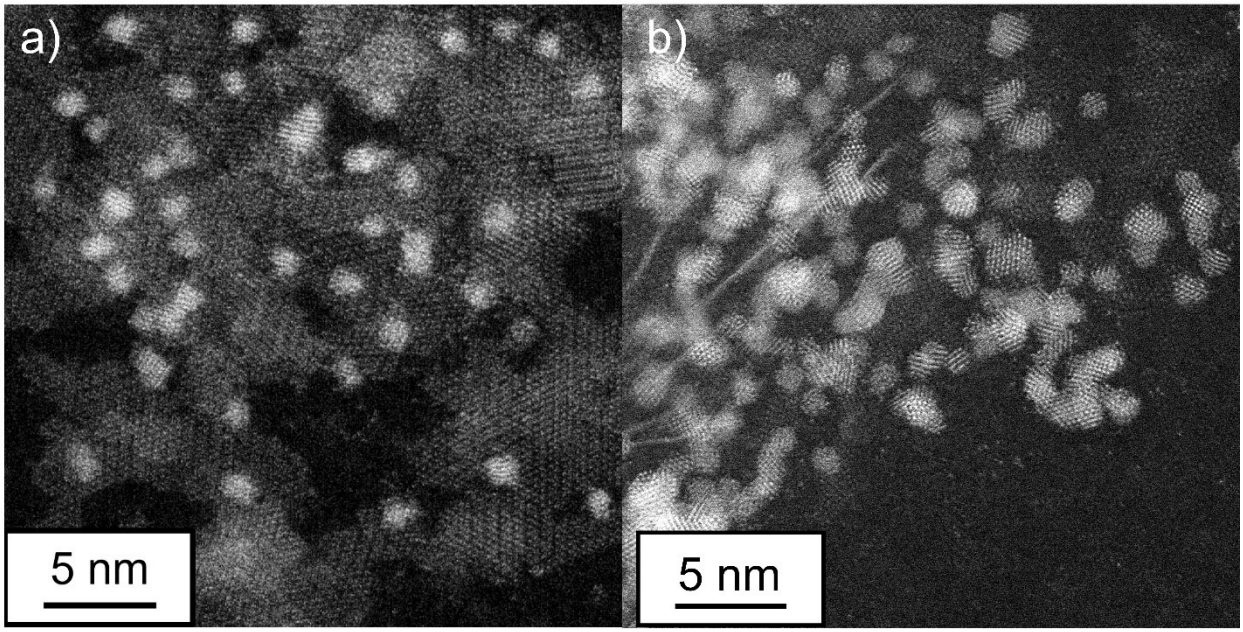

Fig. S19 HAADF-STEM images of the Ir/WS_2 after (a) HER and (b) OER

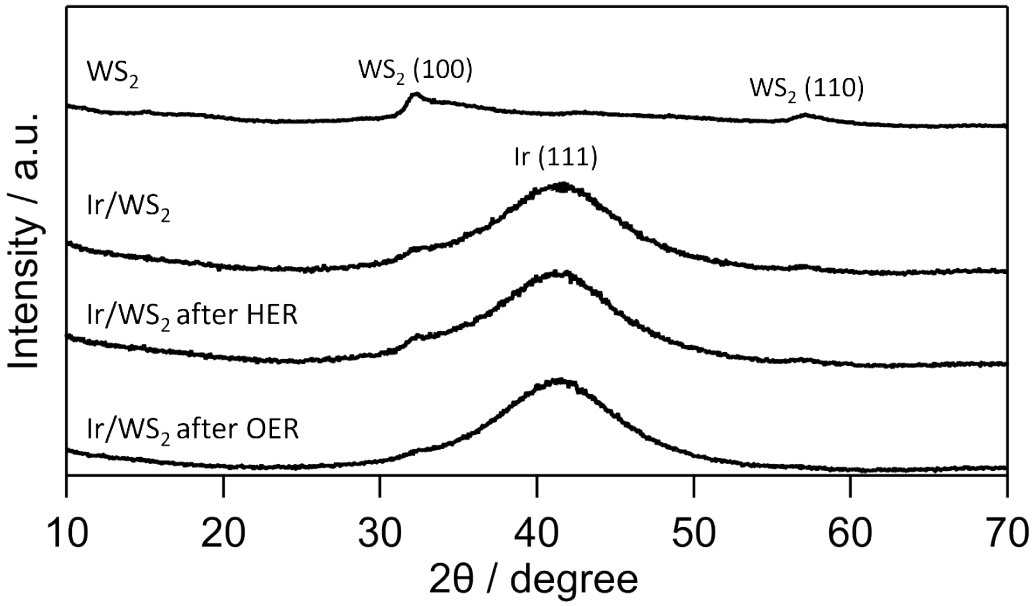

Fig. S20 XRD patterns of Ir/WS_2 before and after HER and OER under the neutral condition.

We conducted the XRD measurements for the samples before and after HER and OER in the neutral media. Before the reaction, the Ir/WS_2 showed the XRD patterns assignable to WS_2 and face-centered cubic (fcc) Ir. After HER, the Ir/WS_2 showed a similar pattern to that before the reaction. However, decreases in the peak intensity of WS_2 at 32˚ and 57˚ were observed after OER. These were consistent with the results from STEM observation, i.e., negligible changes in the Ir/WS_2 after HER and the dissolution of WS_2 in the Ir/WS_2 after OER in Fig. S19. Thus, the XRD measurements also revealed the durability under the HER conditions and instability under the OER conditions.

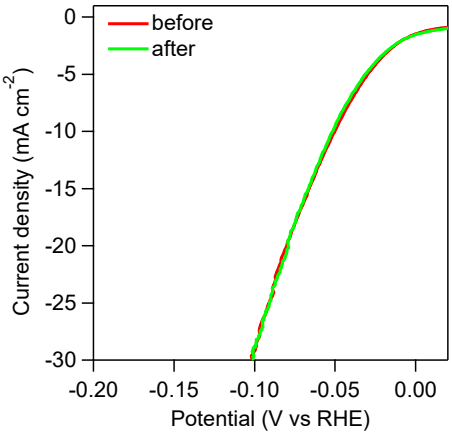

Fig. S21 IR-corrected polarization curves of the Ir/WS_2 for HER in the aqueous solution of 1 mol dm^{-3} PBS before and after 1000 cycle CV durability test.

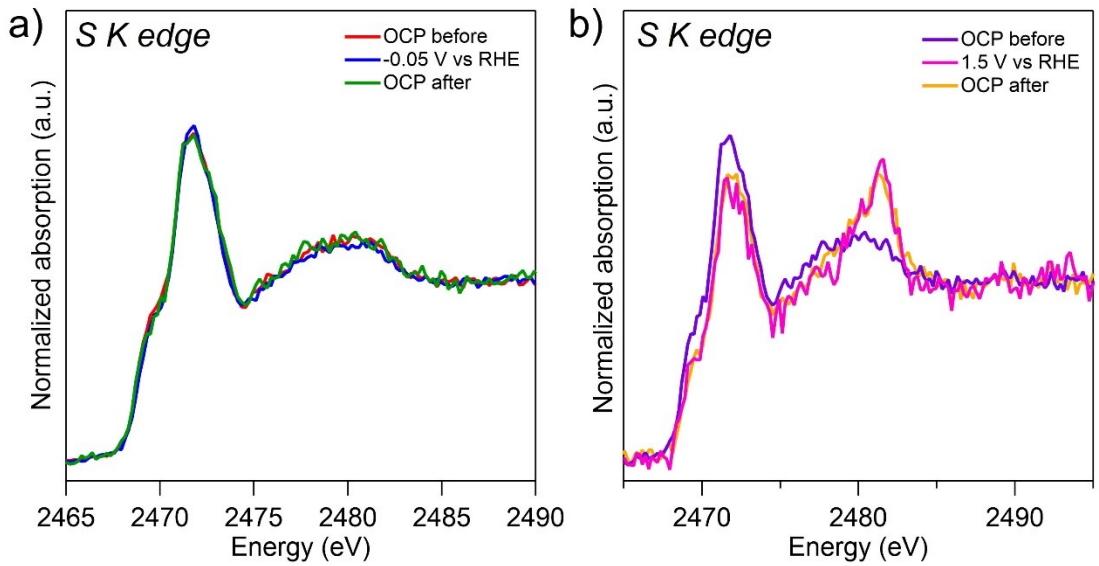

Fig. S22 In situ S K-edge XANES spectra of pristine WS_2 for (a) HER and (b) OER in the aqueous solution of 1 mol dm^{-3} PBS.

The behaviors of pristine WS_2, which does not contain thiosulfate species, were also investigated *in-situ* XAFS measurements. Unlike the Ir/WS_2, the S K-edge spectra did not change under the HER condition, while irreversible oxidative change was observed under the OER condition. Therefore, the results revealed the unique behaviors of thiosulfate species formed at the Ir/WS_2 heterointerface, i.e., promotion of water dissociation under HER conditions.

Table S1 Overpotential of catalysts in HER and OER

	HER (-10 mA cm^{-2})			OER(10 mA cm^{-2})		
Catalyst	Acidic	Neutral	Alkaline	Acidic	Neutral	Alkaline
Ir/WS_2	41.2 mV	50.1 mV	28.7 mV	294 mV	304 mV	285 mV
Ir/G	53.6 mV	109 mV	64.5 mV	311 mV	315 mV	297 mV
Pt/C	26.9 mV	48.4 mV	28.6 mV			
IrO_2				366 mV		357 mV

References

1. Zheng, J.; Zhang, H.; Dong, S. H.; Liu, Y. P.; Nai, C. T.; Shin, H. S.; Jeong, H. Y.; Liu, B.; Loh, K. P., High yield exfoliation of two-dimensional chalcogenides using sodium naphthalenide. *Nat Commun* **2014,** *5*.
2. Fang, J. J.; Wang, H. Y.; Dang, Q.; Wang, H.; Wang, X. D.; Pei, J. J.; Xu, Z. Y.; Chen, C. J.; Zhu, W.; Li, H.; Yan, Y. S.; Zhuang, Z. B., Atomically dispersed Iridium on Mo

C as an efficient and stable alkaline hydrogen oxidation reaction catalyst. *Nat Commun* **2024,** *15* (1).
3. Wang, Q. L.; Xu, C. Q.; Liu, W.; Hung, S. F.; Yang, H. B.; Gao, J. J.; Cai, W. Z.; Chen, H. M.; Li, J.; Liu, B., Coordination engineering of iridium nanocluster bifunctional electrocatalyst for highly efficient and pH-universal overall water splitting. *Nat Commun* **2020,** *11* (1).